

Document downloaded from:

<http://hdl.handle.net/10251/182863>

This paper must be cited as:

Xu, T.; Gómez-Hernández, JJ.; Chen, Z.; Lu, C. (2021). A comparison between ES-MDA and restart EnKF for the purpose of the simultaneous identification of a contaminant source and hydraulic conductivity. *Journal of Hydrology*. 595:1-14.
<https://doi.org/10.1016/j.jhydrol.2020.125681>



The final publication is available at

<https://doi.org/10.1016/j.jhydrol.2020.125681>

Copyright Elsevier

Additional Information

A comparison between ES-MDA and restart EnKF for the purpose of the simultaneous identification of a contaminant source and hydraulic conductivity

Teng Xu^{a,b,c}, J. Jaime Gómez-Hernández^{c,*}, Zi Chen^c, Chunhui Lu^{a,b,*}

^a*State Key Laboratory of Hydrology-Water Resources and Hydraulic Engineering, Hohai University, Nanjing, China*

^b*Yangtze Institute for Conservation and Development, Hohai University, Nanjing, China*

^c*Institute of Water and Environmental Engineering, Universitat Politècnica de València, Valencia, Spain*

Abstract

Understanding a contaminant source may help in a better management and risk assessment of a polluted aquifer. However, contaminant source information may not be available when a pollutant is detected in a drinking well. The restart ensemble Kalman filter (restart EnKF, also named r-EnKF) has been demonstrated in synthetic and laboratory experiments as an efficient solution for the identification of a contaminant source. Recently, the ensemble smoother with multiple data assimilation (ES-MDA) has been proposed as an alternative to the r-EnKF as a more efficient solution given that the r-EnKF needs to restart the simulation of the state equation from time zero after each data assimilation step. An analysis, in a synthetic aquifer, of the accuracy of the ES-MDA for the simultaneous identification of a contaminant source and the spatial distribution of hydraulic conductivity by assimilating both piezometric head and concentration observations is carried out using the r-EnKF as a benchmark. The conclusion is that the ES-MDA can outperform the r-EnKF, but the expected speed advantage, associated with the possibility of assimilating all data at once, does not exist. For the ES-MDA to reach the same level of accuracy as the r-EnKF, the

*Corresponding author

Email addresses: teng.xu@hhu.edu.cn (Teng Xu), jgomez@upv.es (J. Jaime Gómez-Hernández), dtpenguincz@gmail.com (Zi Chen), clu@hhu.edu.cn (Chunhui Lu)

number of multiple data assimilations must be large, and final computing time is similar for both approaches. However, the ES-MDA can do much better than the r-EnKF if the number of iterations increases even further, with the consequent increase of computational cost.

Keywords: Contaminant source identification; Data assimilation; Ensemble smoother with multiple data assimilation; Restart ensemble Kalman filter

1. Introduction

When a contaminant is released into the subsurface, it will jeopardize not only human health but also damage the local ecosphere, especially if the contaminant is hazardous. When contamination happens inadvertently or is purposely hidden, it may be difficult to trace it back from concentration observations taken downstream from the source. Yet, knowledge of the contaminant source is vital for groundwater contamination management, contamination control, contamination risk assessment and remediation.

How to identify a contaminant source once contamination has been detected has attracted much attention in the last decades. It is an intricate problem that has been addressed using inverse modeling. According to their characteristics, the inverse modeling approaches for contaminant source identification could be classified into three categories: optimization approaches, probabilistic approaches, and deterministic approaches. The reader is referred to the reviews by Sun et al. (2006a); Atmadja and Bagtzoglou (2001b); Michalak and Kitanidis (2004); Bagtzoglou and Atmadja (2005) for further information.

In the optimization approaches, the objective is to minimize an objective function that measures the differences between simulated concentrations and measurement observations and that is written in terms of the parameters defining the contaminant source. Some of the approaches used are least-squares regression and linear programming (Gorelick et al., 1983), maximization of correlation coefficients (Sidauruk et al., 1998), constrained robust least squares (CRLS) (Sun et al., 2006a), CRLS estimation combined with a branch-and-

bound global optimization (Sun et al., 2006b), evolutionary search algorithms (Mirghani et al., 2009), or hybrid simulation-optimization (Ayvaz, 2016).

In the probabilistic approaches, the objective is, generally speaking, to maximize some posterior probability of the source parameters given the observations. Some approaches used for this purpose are minimum relative entropy (Woodbury and Ulrych, 1996; Woodbury et al., 1998; Cupola et al., 2015), the geostatistical approach (Sun, 2007; Gzyl et al., 2014; Butera et al., 2013), Markov chain Monte Carlo (Wang and Jin, 2013), or Bayesian approaches (Zeng et al., 2012; Zhang et al., 2015; Zanini and Woodbury, 2016).

In the deterministic approaches, the main objective is to solve the advection-dispersion equation backward in time. Some of the approaches employ the marching-jury backward beam equation method (Atmadja and Bagtzoglou, 2001a; Bagtzoglou and Atmadja, 2003), Tikhonov regularization (Skaggs and Kabala, 1994; Neupauer et al., 2000), or a quasi-reversibility method together with minimum relative entropy (e.g., Skaggs and Kabala, 1995; Bagtzoglou and Atmadja, 2003; Neupauer et al., 2000).

In addition to the approaches mentioned above, recently, the use of the restart ensemble Kalman filter (r-EnKF) (a probabilistic approach), was proposed by Xu and Gómez-Hernández (2016) to identify a contaminant source by assimilating concentration observations. The good results obtained by the r-EnKF in standard inversion problems (e.g., Hendricks Franssen and Kinzelbach, 2009; Xu et al., 2013; Xu and Gómez-Hernández, 2015b) prompted its use for source identification, where it proved to achieve good results, too. Later, Xu and Gómez-Hernández (2018) extended their work to jointly identify the source information and the underlying hydraulic conductivity field in a synthetic aquifer, and in a tank experiment (Chen et al., 2018). Their works have proven the capability of the r-EnKF for contaminant source identification.

The ensemble smoother (ES), also a probabilistic approach, first proposed by Van Leeuwen and Evensen (1996), is an alternative that could alleviate the computational burden of the

47 EnKF, because it assimilates all data for all time steps at once. This avoids the restart of
48 the simulation at every time step and makes the ES faster and easier to implement than the
49 EnKF (Emerick and Reynolds, 2013a). However, the performance of the ES for the case of
50 non-linear state equations is not good (e.g., Evensen and Van Leeuwen, 2000; Crestani et al.,
51 2013), the main reason being the lack of multiple updatings inherent to the EnKF (the ES
52 does only one update).

53 A detailed explanation of why the EnKF outperforms the ES in dealing with non-linear
54 problems can be found in the work by Evensen (2018). Here, a brief explanation is given.
55 The updating step in both the EnKF and the ES are written in terms of covariances, which
56 can only capture linear relationships. The EnKF recursively updates the parameters of
57 interest by assimilating observation information in time and after each step the updates get
58 closer to the reference solution. The ES makes a single update using all the data from all
59 time steps. That is, the EnKF is equivalent to making many linear approximations to the
60 state equation followed by incremental updates along the linear approximation, whereas the
61 ES is equivalent to a single linear approximation to the state equation and a single large
62 update along the linear approximation. Therefore, the EnKF is equivalent to a non-linear
63 optimization based on local linear approximations, whereas the ES is a linear minimization,
64 which may be very far from optimal if the state equation is highly nonlinear. Unless, iteration
65 is also introduced into the ES. This is what Emerick and Reynolds (2013a) propose with
66 their ensemble smoother with multiple data assimilation (ES-MDA). The basic idea is to
67 assimilate all data from all time steps several times, progressively updating the parameters
68 after each iteration.

69 Several successful applications of the ES-MDA are reported in the reservoir history-
70 matching literature (e.g., Emerick et al., 2013; Emerick and Reynolds, 2013b; Le et al., 2015,
71 2016; Lee et al., 2013; Fokker et al., 2016). In these works, the reservoir state equations
72 are nonlinear, and the ES-MDA results outperforms the EnKF for both synthetic and real

73 field problems. Recently, a few applications have been reported in the hydrogeology litera-
74 ture (Li et al., 2018a,b) for the characterization of hydraulic conductivities by assimilating
75 piezometric heads.

76 In this paper, the ES-MDA is used, for the first time, to the best of our knowledge, to
77 jointly identify a heterogeneous hydraulic conductivity field and contaminant source informa-
78 tion on a synthetic aquifer. As a benchmark, the accuracy of the ES-MDA will be compared
79 with the r-EnKF. Note that the main aim of this work is to evaluate the capabilities of the
80 ES-MDA and to benchmark it against the r-EnKF for the joint identification of conductivity
81 field and contaminant source information.

82 The paper is organized as follows. First, we introduce the algorithmic description of the
83 r-EnKF and the ES-MDA. Second, we test and compare the ES-MDA with the r-EnKF on
84 a synthetic aquifer. And third, we discuss the results.

85 **2. Methodology**

86 *2.1. Restart ensemble Kalman filter*

87 The EnKF was developed based on the Kalman filter proposed by Kalman et al. (1960)
88 to better tackle nonlinear state-transfer equations. The main difference between the EnKF
89 and the Kalman filter is on how the covariance matrices are calculated. In the original filter,
90 the covariances were propagated in time using a linear state-transfer function (or a linear
91 approximation in case the function is non-linear), while in the EnKF, the covariances are
92 calculated from the states obtained after solving the state-transfer function on an ensemble
93 of realizations (e.g., Evensen, 2003, 2009; Chen and Zhang, 2006; Xu et al., 2013; Xu and
94 Gómez-Hernández, 2015a). Like the Kalman filter, the EnKF consists of two steps: forecast
95 and analysis. The first one is to forecast the state variables from the state variables and
96 the best estimate of the model parameters from the last time step. And the second one
97 is to update the state variables and model parameters at the current time step based on

98 the deviations between forecasted and observed state variable values at selected observation
99 points. However, as already discussed in Xu and Gómez-Hernández (2016), it is impossible
100 to take into account the updated parameters in the forecast step when these parameters
101 define the spatiotemporal position of a contaminant source, unless the forecast is restarted
102 from time zero. This approach modifies the standard Kalman filter equations since there is
103 no need to update the variable values at the analysis step: their values will be recomputed
104 with the new estimates of the model parameters from times zero.

105 For any given realization of the ensemble, let V_t^f denote the forecasted state variables at
106 time t , and S_t^a the best model parameter estimates after the analysis step at the same time.
107 The forecast equation is

$$V_t^f = \psi(V_0, S_{t-1}^a). \quad (1)$$

108 where ψ represents the state-transfer function, and V_0 represents the state variables at time
109 zero. The update step modifies the parameter values from the previous time step (S_{t-1}^a) as
110 a function of the discrepancy between forecasted and observed state variables at observation
111 locations

$$S_t^a = S_{t-1}^a + G_t^f (V_{o,t} + e_t - V_{o,t}^f) \quad (2)$$

112 with

$$G_t^f = D_{SV,t}^f (D_{VV,t}^f + R_t)^{-1}, \quad (3)$$

113 where $V_{o,t} + e_t$ is the vector of observed concentrations and piezometric heads (composed of
114 the sum of the true head or concentration $V_{o,t}$ plus an observation error e_t of zero mean and
115 covariance R_t), G_t^f is the Kalman gain, $D_{SV,t}^f$ is the cross-covariance between parameters and
116 forecasted state variables at observation locations, and $D_{VV,t}^f$ is the auto-covariance between
117 the forecasted state variables at the observation locations.

118 Consider that there are N_r realizations in the ensemble and each realization has been
119 discretized into N_e elements. The state variable vector V contains piezometric heads H and

120 concentrations C at all aquifer model cells

$$V = \begin{bmatrix} H \\ C \end{bmatrix}. \quad (4)$$

121 This vector contains N_r realizations of $2N_e$ variables.

122 The model parameter vector S contains hydraulic log-conductivity $\ln K$ in all aquifer
 123 model cells and the contaminant source parameters, which are source location, X for the
 124 x -coordinate, and Y for the y -coordinate, initial release time T , release duration ΔT , and
 125 mass-loading rate M

$$S = \begin{bmatrix} \ln K \\ X \\ Y \\ T \\ \Delta T \\ M \end{bmatrix}. \quad (5)$$

126 This vector contains N_r realizations of $(N_e + 5)$ variables.

127 Then, if we define $d_t = V_{o,t} + e_t - V_{o,t}^f$ and $P_{VV,t}^f = (D_{VV,t}^f + R_t)^{-1}$, and the covariances
 128 are split into the auto- and cross- covariances of each parameter, the updating equation (2),
 129 applicable to each realization independently, can be written as

$$S_t^a = \begin{pmatrix} \ln K \\ X \\ Y \\ T \\ \Delta T \\ M \end{pmatrix} + \begin{pmatrix} D_{(\ln K)C,t}^f & D_{(\ln K)H,t}^f \\ D_{XC,t}^f & D_{XH,t}^f \\ D_{YC,t}^f & D_{YH,t}^f \\ D_{TC,t}^f & D_{TH,t}^f \\ D_{(\Delta T)C,t}^f & D_{(\Delta T)H,t}^f \\ D_{MC,t}^f & D_{MH,t}^f \end{pmatrix} \begin{pmatrix} P_{CC,t}^f & P_{CC,t}^f \\ P_{HC,t}^f & P_{HC,t}^f \end{pmatrix} \begin{pmatrix} d_{C,t} \\ d_{H,t} \end{pmatrix} \quad (6)$$

130 *2.2. Ensemble smoother with multiple data assimilation*

131 The ES is, conceptually, the same as the r-EnKF but limited to one forecast step (for all
 132 the time steps for which observations are available) and a single update step (based on the
 133 discrepancies between observations and predictions at all time steps).

134 The equations that describe the ES are almost the same as those for the r-EnKF above,
 135 with some differences. The forecast step is given by

$$V^f = \psi(V_0, S_0). \quad (7)$$

136 where now V^f contains the state forecasted at all time steps —computed from the initial
 137 state V_0 and the initial ensemble of parameters S_0 . And the update step is given by

$$S^a = S_0 + G^f(V_o + e - V_o^f), \quad (8)$$

138 with

$$G^f = D_{SV}^f (D_{VV}^f + R)^{-1}, \quad (9)$$

139 where $V_o + e$ are all of the observations at observation locations, e are the observation
 140 errors, and V_o^f are the forecasts at observation locations. The covariances appearing in Eq.
 141 (9), D_{SV}^f and D_{VV}^f are computed for all time steps; these covariance matrices include the
 142 cross-covariances between time steps, an aspect not accounted for in the r-EnKF that might
 143 render the ES superior to the r-EnKF. From a computational point of view, if there are N_o
 144 observations locations sampled N_t times, the sizes of the matrices involved in the r-EnKF are
 145 proportional to N_o , whereas in the ES they are proportional to the product $N_o \cdot N_t$. Hence,
 146 the sizes of the cross-covariances in the r-EnKF are $(N_e + 5) \times 2N_o$ for $D_{SV,t}^f$, and $2N_o \times 2N_o$
 147 for $D_{VV,t}^f$ and R_t ; whereas the size of the cross-covariance for the ES are $(N_e + 5) \times (2N_o \cdot N_t)$
 148 for D_{SV}^f and $(2N_o \cdot N_t) \times (2N_o \cdot N_t)$ for D_{VV}^f and R .

149 As we stated before, the performance of the ES is not good when dealing with non-
150 linear problems. The solution provided by Emerick and Reynolds (2013a) to improve the
151 performance of the ES for non-linear state-transfer equations is to iterate, what is called
152 multiple data assimilation (because the same data is assimilated multiple times) on the basis
153 that each iteration of the ES is similar to a Gauss-Newton iteration (Reynolds et al., 2006;
154 Gu and Oliver, 2007). Basically, Eq. (7) and Eq. (10) are iteratively applied using the
155 latest updated parameters as the initial parameters for the next iteration. However, since
156 all data are assimilated multiple times, there is a need to inflate the observation error for
157 each assimilation step. For this purpose, a non-increasing sequence of error variance inflation
158 coefficients $\{a_i, i = 1, \dots, N_a\}$ is used in the updating equations, with N_a being the number
159 of assimilation iterations, and satisfying that $\sum_{i=1}^{N_a} \frac{1}{a_i} = 1$.

160 The ES-MDA equations display the following differences. The forecast step is given by

$$V_i^f = \psi(V_0, S_i^a). \quad (10)$$

161 where i is the iteration counter, and for each iteration the forecast uses the last updated
162 parameters from the previous iteration. And the update equation is given by

$$S_i^a = S_{i-1}^a + G_i^f (V_{o,i} + \sqrt{a_i} e_i - V_{o,i}^f) \quad (11)$$

163 with

$$G_i^f = D_{SV,i}^f (D_{VV,i}^f + a_i R_i)^{-1}, \quad (12)$$

164 In Eq. (11) and Eq. (12), we can see how the observation variance is amplified by a
165 factor a_i and the observation error is amplified by $\sqrt{a_i}$.

166 If we define $d_i = V_{o,i} + \sqrt{a_i} e_i - V_{o,i}^f$ and $P_{VV,i}^f = (D_{VV,i}^f + a_i R_i)^{-1}$, and the covariances are
167 split into the auto- and cross- covariances of each parameter, the updating equation Eq.(8)

168 can be written as

$$S_i^a = \begin{pmatrix} \ln K \\ X \\ Y \\ T \\ \Delta T \\ M \end{pmatrix} + \begin{pmatrix} D_{(\ln K)C,i}^f & D_{(\ln K)H,i}^f \\ D_{XC,i}^f & D_{XH,i}^f \\ D_{YC,i}^f & D_{YH,i}^f \\ D_{TC,i}^f & D_{TH,i}^f \\ D_{(\Delta T)C,i}^f & D_{(\Delta T)H,i}^f \\ D_{MC,i}^f & D_{MH,i}^f \end{pmatrix} \begin{pmatrix} P_{CC,i}^f & P_{CC,i}^f \\ P_{HC,i}^f & P_{HC,i}^f \end{pmatrix} \begin{pmatrix} d_{C,i} \\ d_{H,i} \end{pmatrix} \quad (13)$$

169 Please notice that, when $N_r < 2N_o$ in r-EnKF, or $N_r < 2N_o \times N_t$ in ES-MDA, the
 170 low rank of the matrices prevent their inversion; then, the subspace inversion introduced by
 171 Evensen (2004) is used to solve for $P_{VV,t}^f$ or $P_{VV,i}^f$. The detailed explanation can be found in
 172 the works by Evensen (2004); Emerick and Reynolds (2013a).

173 3. Application

174 A synthetic confined aquifer is designed and constructed on a 1000 [L] by 1000 [L] by 50
 175 [L] prism discretized into 50 by 50 by 1 cells, where each cell is 20 [L] by 20 [L] by 50 [L].
 176 (Please note that no specific units are used throughout, only their dimensional analysis is
 177 given. Any set of consistent units will yield the same results.) The reference log-conductivity
 178 field is drawn from a multivariate Gaussian random function defined by the parameters in
 179 Table 1 using the GCOSIM3D software —a sequential Gaussian simulation program (Gómez-
 180 Hernández and Journel, 1993). The resulting reference log-conductivity field is shown in
 181 Figure 1.

Table 1: Parameters of the random functions used to generate the $\ln K$ realizations. Spherical variogram with anisotropic spatial correlation defined by λ_{max} and λ_{min} , which are the ranges in the maximum and minimum directions of continuity. The angle corresponds to the maximum continuity direction and it is measured clockwise from the North direction

	Mean	Std. dev.	Variogram	λ_{max}	λ_{min}	Angle
$\ln K$	-1	1	Spherical	300	200	135

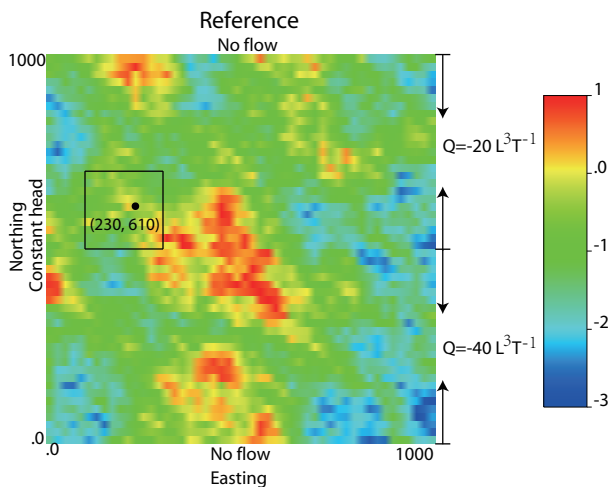


Figure 1: Reference $\ln K$ and boundary conditions. The source location is marked with a dark dot. The inner square indicates the suspect contaminant source.

182 The model boundaries, as indicated in Figure 1, are set as follows: north and south
 183 boundaries are impermeable; west boundary is a prescribed head condition with a constant
 184 value of 50 [L]; east boundary is a prescribed flow boundary divided into two equal-length
 185 segments: the north segment with a total prescribed flow extraction rate of 20 [$L^3 T^{-1}$] and
 186 the south segment with a total extraction prescribed flow rate of 40 [$L^3 T^{-1}$]. Figure 2 shows
 187 the location of the 25 observation wells (red triangles) and the two verification wells (blue
 188 diamonds).

189 The initial concentration is zero [ML^{-3}] and the initial head for the whole domain is 58 [L],
 190 except at the west constant boundary. Other groundwater flow and contaminant transport

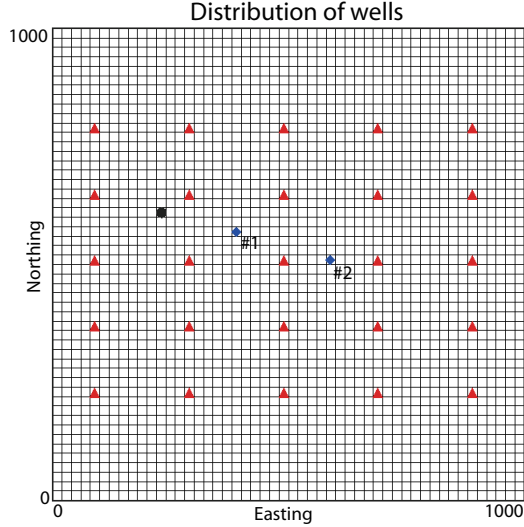


Figure 2: Location of wells. Red triangles mark observation wells; blue diamonds mark verification wells. The black circle is the contaminant source location.

191 parameters are assumed known and set as homogeneous: porosity of 0.3 [–], longitudinal
 192 dispersivity of 2 [L], transverse to longitudinal dispersivity ratio of 0.1.

193 We assume the contaminants are inert. Only advection and dispersion are considered
 194 as transport mechanisms. Both groundwater flow and contaminant transport are under
 195 transient conditions. The groundwater flow simulator MODFLOW (McDonald and Har-
 196 baugh, 1988) and the transport simulator MT3DMS (e.g., Zheng, 2010; Ma et al., 2012) are
 197 used as forward models to solve the groundwater flow and contaminant transport problems,
 198 respectively.

199 The total simulation time is 10000 [T] and is discretized into 100 time steps with in-
 200 creasing size following a geometric series with ratio 1.01 (The first time step is 58.66 [T]).
 201 The observations of both piezometric head and concentration from the first 60 time steps
 202 (around 4790 [T]) are assimilated for the purpose of parameter identification, so the total
 203 number of observations is $2 \times 25 \times 60$.

204 The contaminant is released at location $(X, Y) = (230, 610)$ [L] with a mass-loading rate
 205 of 1000 [MT⁻¹], starting at time 613 [T] (around the 10th time step) and ending at time

206 2867 [T] (around the 40th time step), with a release duration of 2254 [T].

207 Figure 3 shows three snapshots of piezometric head and solute concentration taken on the
 208 reference aquifer at the 10th simulation time step (beginning of contaminant injection), 40th
 209 time step (end of contaminant injection), and at 60th time step (end of assimilation period).
 210 This figure also shows the location where both piezometric heads and concentrations are
 211 sampled for the purpose of their assimilation in the different scenarios described next.

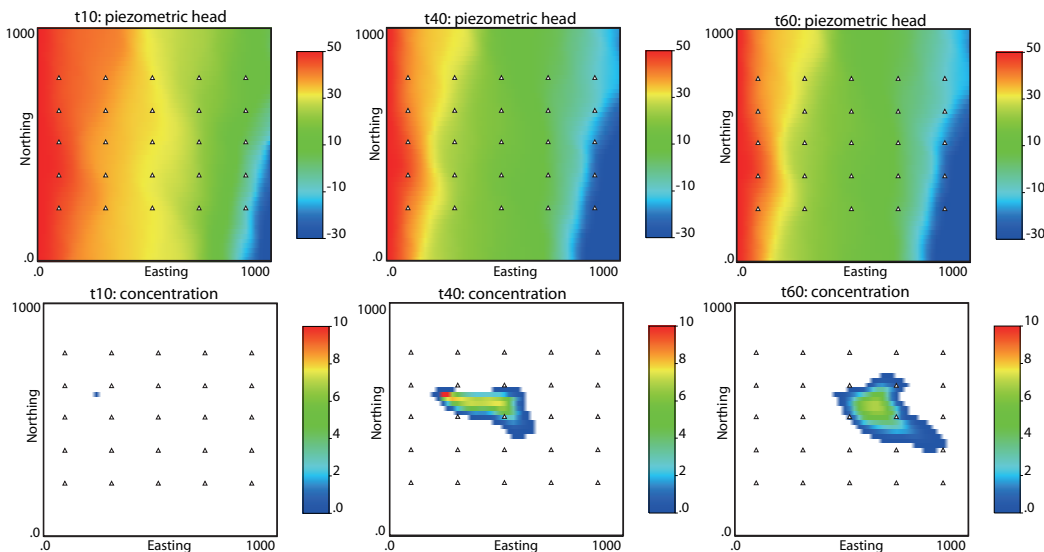


Figure 3: Reference. Piezometric head (top row) and contaminant plume (bottom row) at the 10th (beginning of solute injection), 40th (end of solute injection), and 60th (end of assimilation) time steps in the reference aquifer. White triangles mark the observation wells.

212 Seven scenarios will be evaluated. The first one, used as a benchmark to evaluate the
 213 efficiency of the ES-MDA, is the r-EnKF, which has already proven its ability for the iden-
 214 tification of contaminant source parameters and hydraulic conductivity characterization; it
 215 will be referred to as S0. The second one is the ES in its original implementation, that is,
 216 without any iteration. Then, to evaluate the effect of the number of iterations, the ES-MDA
 217 is run for five different scenarios, the difference between them is the number of iterations
 218 (or data assimilations) performed; they will be labeled S2 to S6 with 2, 4, 6, 8 and 10 it-
 219 erations, respectively. Notice that the observation error inflation coefficients a_i will, in all

220 cases, be equal to the number of iterations, following the recommendations by Emerick and
221 Reynolds (2013a), who show that the use of decreasing inflation coefficients leads to only
222 small improvements with respect to using the inflation coefficients equal to the number of
223 iterations.

224 As we stated before, the total number of cells of the log-conductivity field is 50×50 , and
225 the number of source parameters is 5, so the total number of parameters to be identified is
226 2505. An ensemble of 400 initial log-conductivity realizations is generated using the same
227 random function model and parameters as for the reference log-conductivity field. The
228 number of ensemble members was chosen after a previous analysis with ensemble sizes of
229 200, 400 and 800 members. The difference in results between the ensemble sizes of 400 and
230 800 were not large enough to grant the use of the largest ensemble. Notice that there are
231 no conditioning log-conductivity data, thus the ensemble mean and ensemble variance of
232 the initial log-conductivity realizations are homogeneous and equal to their marginal values.
233 As already discussed by Xu et al. (2013) the use of the same random function parameters
234 for the generation of the initial realizations as for the generation of the reference case is
235 only a marginal advantage given that there are no conditioning conductivities. Indeed,
236 Xu et al. (2013) demonstrate the effectiveness of the r-EnKF using a totally uninformative
237 prior random function for the generation of the initial ensemble, with similar results as
238 when the “true” random function is used. In addition, an ensemble of 400 5-tuplets for the
239 source parameters is generated, each 5-tuplet contains five values drawn independently from
240 the following uniform distributions: initial release time $T \in \mathcal{U}[550, 750]$, release duration
241 $\Delta T \in \mathcal{U}[2100, 2300]$, mass-loading rate $M \in \mathcal{U}[900, 1100]$, and source location $(X, Y) \in$
242 $(\mathcal{U}[100, 300] \times \mathcal{U}[500, 700])$.

243 **4. Results**

244 Before starting the analysis of the results, Table 2 shows the CPU consumption for all
 245 scenarios. Recall that in the r-EnKF (S0) there are 60 forecasting steps starting from time
 246 0, and 60 assimilation steps to update the parameters 60 times based on the observations
 247 at 25 wells; whereas, in the ES-MDA the number of model runs for the whole simulation
 248 period is equal to the number of assimilation steps, but at each assimilation step, there are
 249 1500 observations (25 observation locations times 60 time steps). For the current model and
 250 setup, the ES-MDA is cheaper to run than the r-EnKF up until data are assimilated four
 251 times. When ten iterations are performed, the ES-MDA costs two and half times that of the
 252 r-EnKF.

Table 2: Definition of scenarios and CPU time consumption. The number in parenthesis refers to the number of data assimilation steps used in the ES-MDA. (ES would be equivalent to ES-MDA(1))

Method	Scenario	CPU in s	CPU in % of S0
r-EnKF	S0	16366	100%
ES	S1	4981	30%
ES-MDA(2)	S2	9526	58%
ES-MDA(4)	S3	17937	110%
ES-MDA(6)	S4	27432	149%
ES-MDA(8)	S5	34936	210%
ES-MDA(10)	S6	42422	259%

253 The r-EnKF, the ES and the ES-MDA will be used to assimilate the piezometric head
 254 and concentration data at the 25 observation locations. This assimilation will result in an
 255 ensemble of updated parameters (for the spatial distribution of hydraulic conductivity and
 256 for the parameters defining the contaminant source) that are used to produce an ensemble

257 of piezometric heads and concentrations past the assimilation period (60th time step) for 40
 258 time steps more. The performance of the different scenarios will be evaluated by comparing
 259 the different final ensembles to their corresponding counterparts in the reference aquifer.

260 Figure 4 shows the ensemble mean and the ensemble variance of the updated log-conductivities
 261 for scenarios S0 to S3 and S6. (The corresponding maps for S4 and S5 for this and following
 262 figures are shown in the appendix.) The ensemble mean shows how the main patterns of
 263 variability of the reference are captured by the updated ensemble, and the ensemble variance
 264 shows the local variability of the updated log-conductivities. From a purely qualitative point
 265 of view it is clear that the r-EnKF does a good job in capturing the reference patterns with
 266 a small local uncertainty where the ensemble variance is close to zero, that the ES is able to
 267 extract patterns which are, overall, similar to the reference but still far from them and with
 268 a substantial local uncertainty, and that the ES-MDA gets better the more times data are
 269 assimilated, with scenario S6 —for which data are assimilated 10 times— giving the best
 270 results.

271 The above analysis can be quantified by computing the average absolute bias (AAB) and
 272 the ensemble spread (ESp). The AAB is used to measure the average absolute deviation
 273 between the updated values and the reference ones. The ESp measures the precision of the
 274 ensemble of updated realizations by calculating the root square of the ensemble variance.
 275 Their expressions are the following

$$\text{AAB} = \frac{1}{N_e} \sum_{i=1}^{N_e} \frac{1}{N_r} \sum_{j=1}^{N_r} |\ln K_{i,j} - \ln K_{i,ref}|, \quad (14)$$

276

$$\text{ESp} = \sqrt{\frac{1}{N_e} \sum_{i=1}^{N_e} \sigma_i^2}, \quad (15)$$

277 where N_e is the number of model elements, N_r is the number of realizations, $\ln K_{i,ref}$ is
 278 the reference log-conductivity value at node i , $\ln K_{i,j}$ is the log-conductivity at node i for

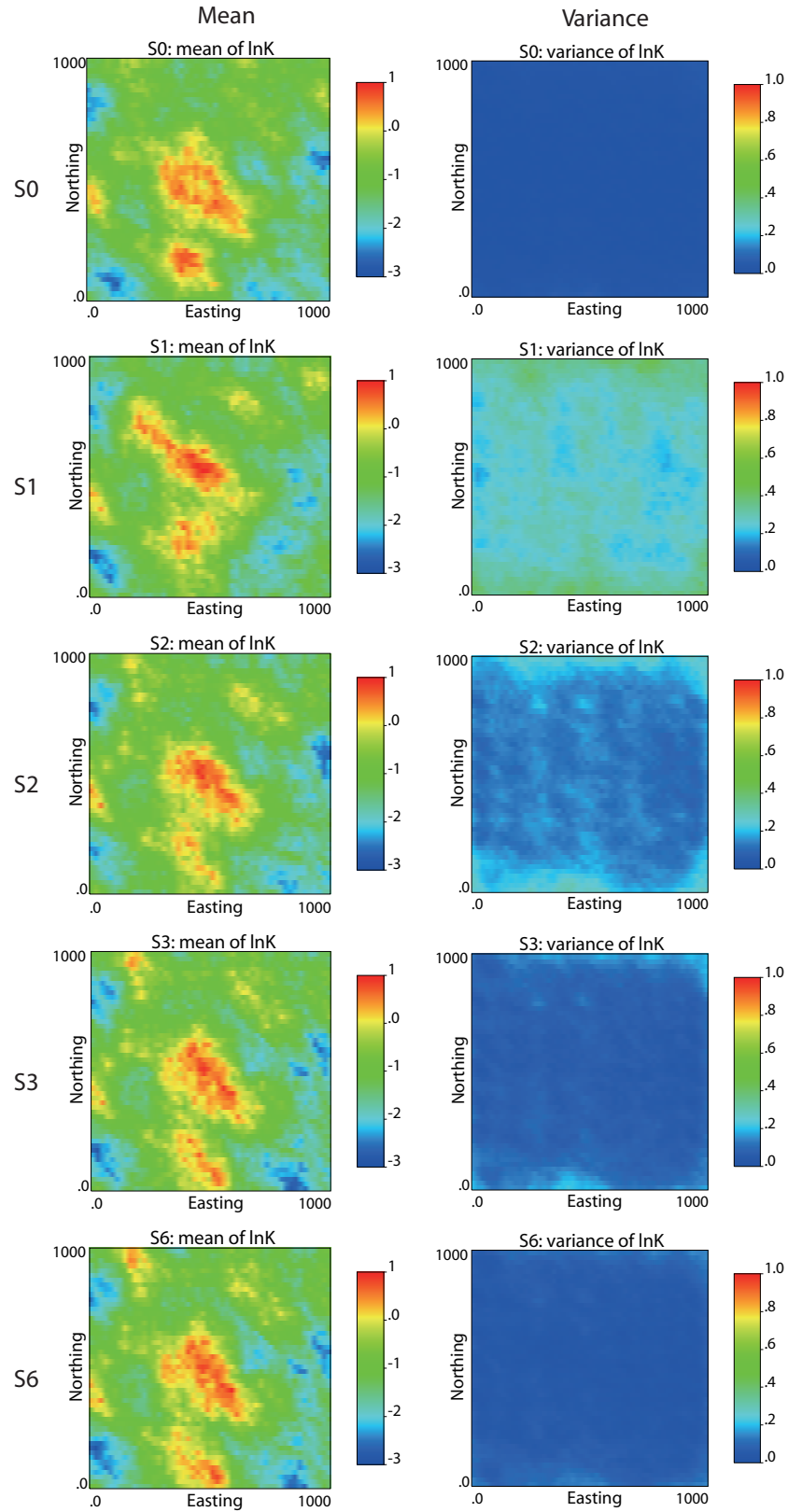


Figure 4: Scenarios S0-S3 and S6. Ensemble mean (left column) and ensemble variance (right column) of updated log-conductivity realizations.

279 realization j and σ_i is the log-conductivity ensemble variance at node i .

280 Figure 5 shows the AAB and ES_p of $\ln K$ and of the parameters defining the contaminant
 281 source for all scenarios, computed before any data assimilation and after data have been
 282 assimilated over the first 60 time steps. The values, as expected, are the highest for the
 283 initial ensembles. They are drastically reduced for the r-EnKF except for ΔT and M . The
 284 smoother provides increasingly smaller values as the number of assimilation steps increases,
 285 with the best values for S6 after ten iterations. Specifically, the AAB and ES_p of the updated
 286 $\ln K$, and Y for scenarios S3-S6 is close to that of scenario S0, and the AAB and ES_p of the
 287 updated T for scenario S6 is close to that of scenario S0; while, the AAB and ES_p of the
 288 updated X , ΔT and M of scenarios S3-S6 is smaller than that of scenario S0. From these
 289 results we could conclude that, after four assimilation steps, the ES-MDA starts to perform
 290 better than the r-EnKF.

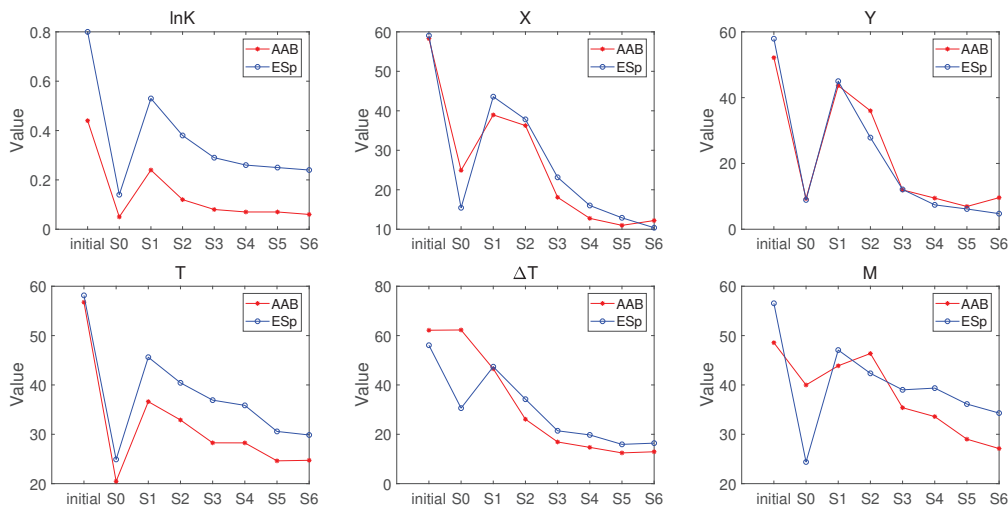


Figure 5: Scenarios S0-S6. Average absolute bias (AAB) and ensemble spread (ES_p) of log-conductivity ($\ln K$), source location (X and Y), initial release time (T), release duration (ΔT), and mass-loading rate (M) computed on the initial parameters and on the updated parameters for the different scenarios after 60 time steps.

291 Figure 6 shows the piezometric head distribution at the 60th time step computed with the
 292 final updated parameters for scenarios S0 to S3 and S6. The maps show, in the left column,

293 the piezometric head distributions for an individual ensemble member (realization #300), in
294 the center column, the ensemble mean obtained as the local mean of the piezometric head
295 at each node through the 400 realizations, and in the right column the ensemble variance.
296 Please, notice that the middle column with the ensemble mean piezometric heads is not the
297 solution of the state equations in the ensemble log-conductivity average of Fig. 4. An analysis
298 of these maps shows the robustness of the r-EnKF (S0) that produces an ensemble mean
299 map quite close to the reference one (upper right corner in Fig. 3) and with little variability
300 everywhere. The smoother performs well when comparing the average ensemble with the
301 reference map, but the uncertainties associated are quite large, especially in scenarios S1 and
302 S2; there is a need to assimilate the data at least four times (S3) to get a variance reduction
303 that approximates that of the r-EnKF.

304 Figure 7 shows the concentration plume computed with the parameters updated using
305 observations at 60 time steps. In the left column, the plume in realization #300, in the
306 center, the ensemble mean of the 400 plumes computed in the 400 realizations with updated
307 parameters, and in the right column the local concentration variance computed at each node
308 through the ensemble of realizations. Please, notice that, as with piezometric heads, the
309 middle column with the ensemble mean concentrations is not the solution of the state equa-
310 tions in the ensemble log-conductivity average of Fig. 4. An analysis of these maps reaches
311 the same conclusions as for the piezometric heads, the r-EnKF is quite robust producing an
312 ensemble mean plume quite close to the reference (lower right corner in Fig. 3) and with
313 lower variability. The smoother performs well only when the number of iterations is large
314 (S3 and S6); for the cases of one, and two iterations (S1 and S2, respectively), the ensemble
315 mean plume is quite spread, the local variance is large, and the plume in the single selected
316 realization shown in the left column of the figure can be quite far from the reference one.

317 Figure 8 shows the time evolution of piezometric heads and solute concentrations at the
318 two verification wells (#1 and #2) computed using the initial ensembles of contaminant

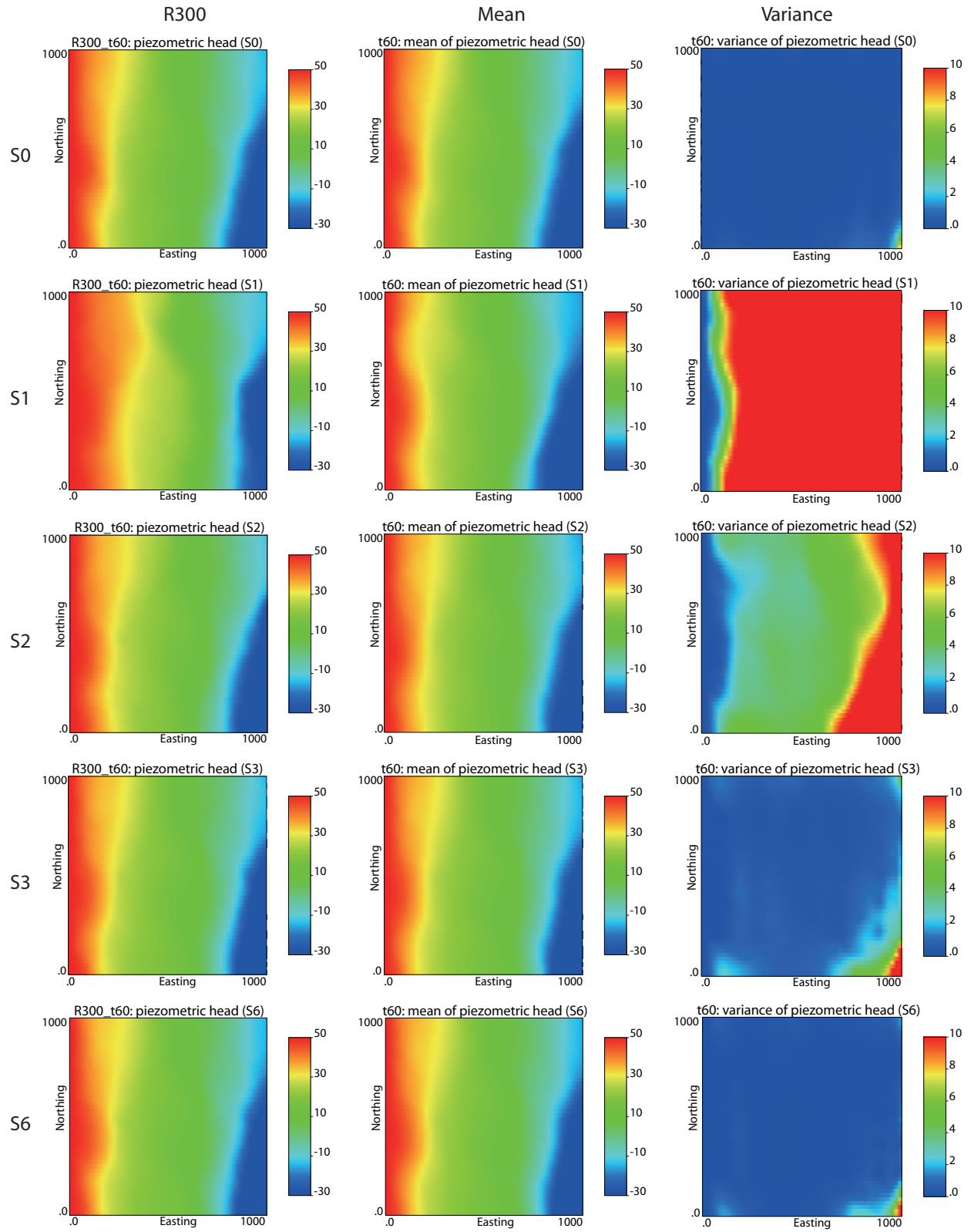


Figure 6: Scenarios S0-S3 and S6. Piezometric heads as computed with the updated parameters at the end of the 60th time step. From left to right, heads in realization #300; ensemble mean, and ensemble variance.

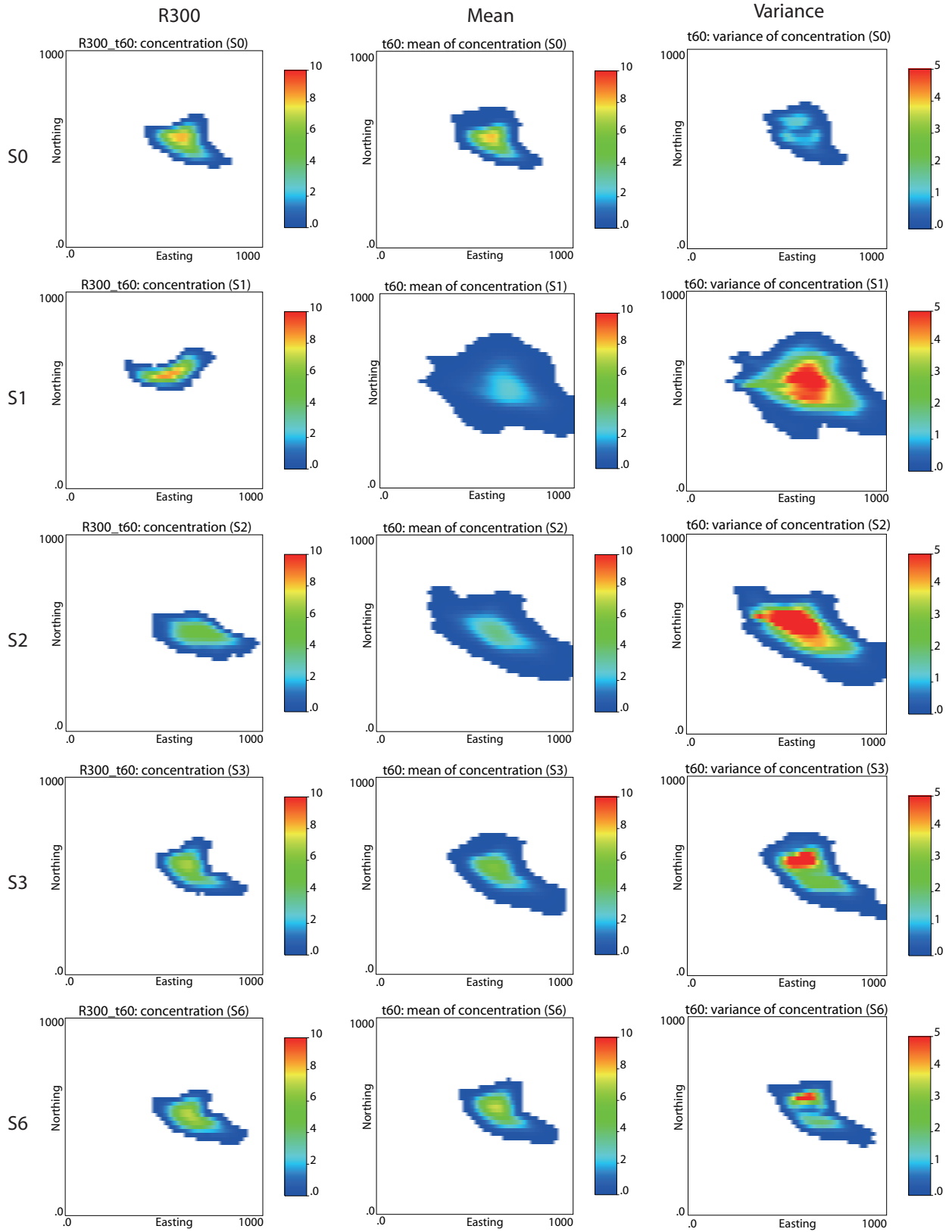


Figure 7: Scenarios S0-S3 and S6. Contaminant plume as computed with the updated parameters at the end of the 60th time step. From left to right, Contaminant plume in realization #300; ensemble mean of all contaminant plumes, and ensemble variance of all contaminant plumes.

319 source parameters and log-conductivities. The spread of predicted values is quite large
 320 since no observation has been assimilated yet. Figure 9 and 10 show the time evolution of
 321 piezometric heads and solute concentrations computed with the updated source parameters
 322 and log-conductivity fields after the assimilation of the observations during the first 60 time
 323 steps, respectively. The spread of the curves after the assimilation is considerably reduced,
 324 especially for scenarios S0, S3 and S6. Although these two wells were not used during the
 325 assimilation, the reproduction of piezometric heads, even after the assimilation period ends
 326 is very good both for the r-EnKF (S0) and for the ES-MDA with four and ten iterations (S3
 327 and S6), with the former performing slightly better than the latter.

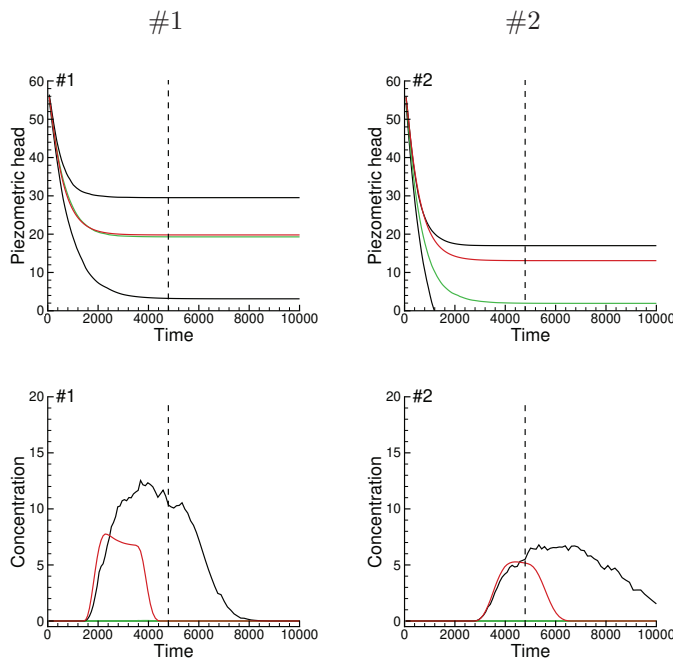


Figure 8: Time evolution of piezometric heads (top row) and solute concentrations (bottom row) at the two verification wells #1, and #2 computed on the initial ensemble of source information parameters and $\ln K$. The red line corresponds to the the reference field. The black lines correspond to the 5 and 95 percentiles of all realizations, and the green line corresponds to the median. The vertical dashed lines mark the end of the assimilation period.

328 Up to here, regarding the characterization of the log-conductivity field and the repro-
 329 duction of the state variables, the r-EnKF seems to outperform the ES-MDA with four

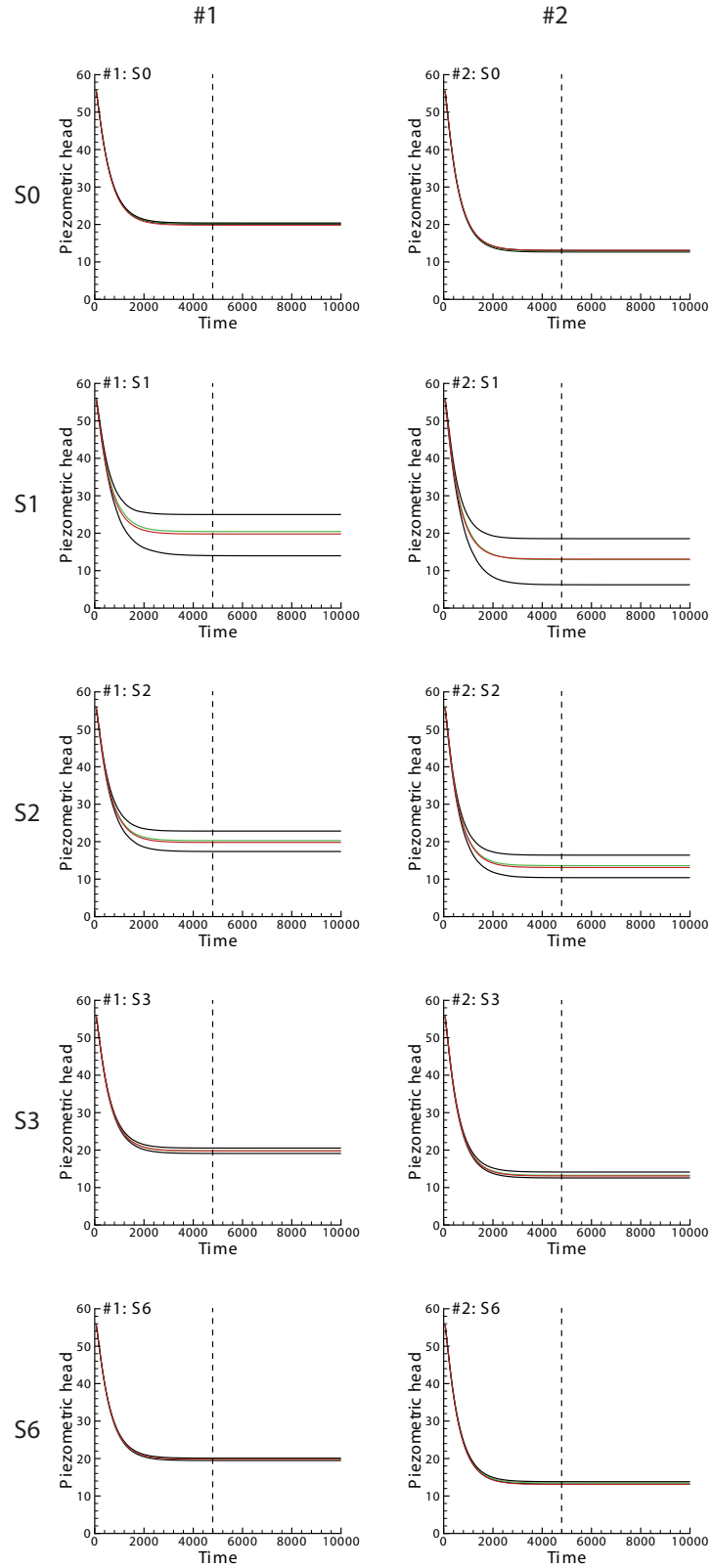


Figure 9: Scenarios S0-S3 and S6. Time evolution of the piezometric heads at the two verification wells #1, and #2 computed with the updated ensemble of source information parameters and $\ln K$ after the assimilation of the observations of the first 60 time steps. The red line is the evolution of the piezometric head in the reference. The black lines correspond to the 5 and 95 percentiles of all realizations, and the green line corresponds to the median. The vertical dashed lines mark the end of the assimilation period.

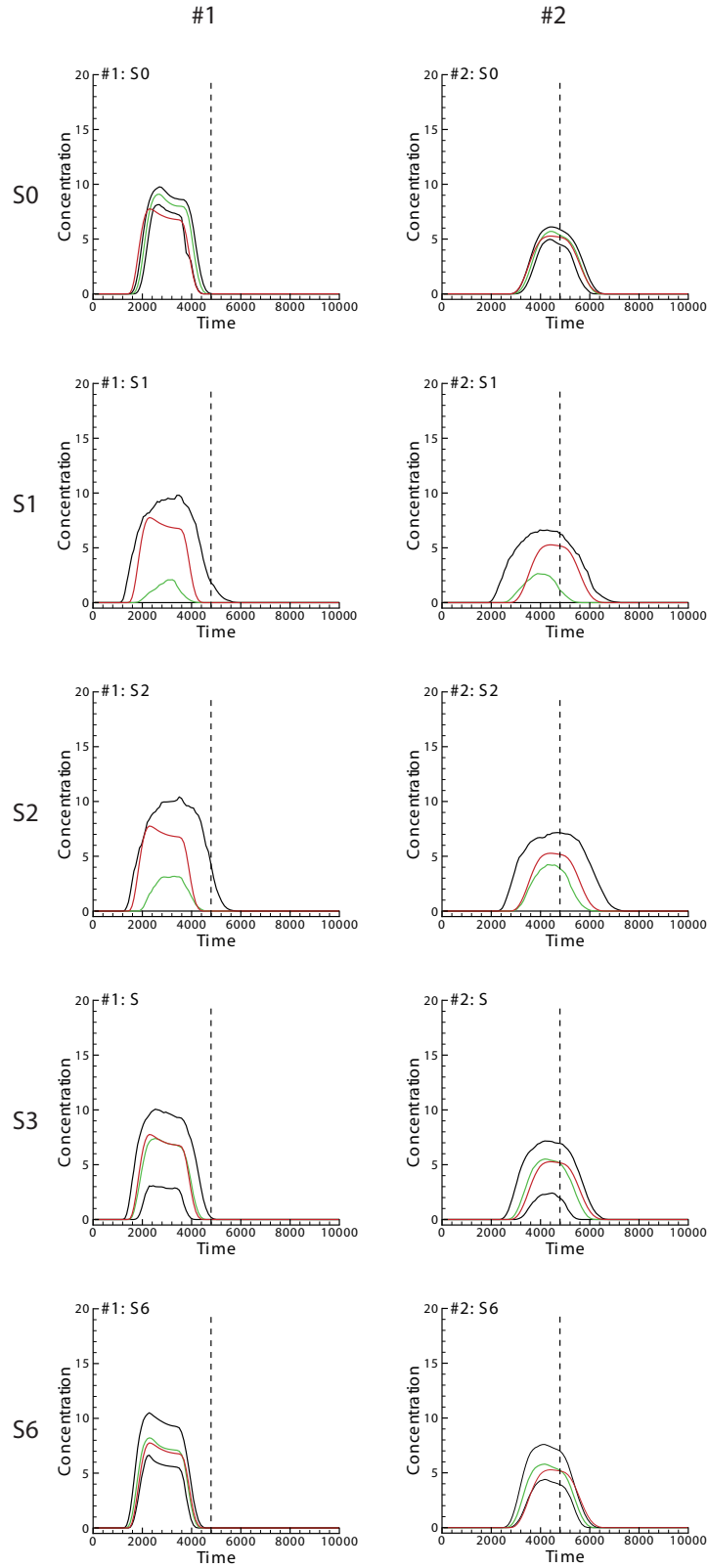


Figure 10: Scenarios S0-S3 and S6. Time evolution of the solute observations at the two verification wells #1, and #2 computed with the updated ensemble of source information parameters and $\ln K$ after the assimilation of the solute observations of the first 60 time steps. The red line is the evolution of the concentration in the reference. The black lines correspond to the 5 and 95 percentiles of all realizations, and the green line corresponds to the median. The vertical dashed lines mark the end of the assimilation period.

330 iterations. The $AAB(\ln K)$ and $ESp(\ln K)$ are the smallest for S0 (r-EnKF), and the piezo-
331 metric head and concentration predictions are also the best for S0. Only the ES-MDA with
332 ten assimilation steps (S6) gives comparable results, although at a CPU cost 2.6 times larger
333 than the r-EnKF.

334 However, when we analyze the reproduction of the contaminant source parameters, we
335 have already discussed Figure 5 showing that the ES-MDA is superior to the r-EnKF. This
336 observation is complemented by the results shown in Figure 11, in which boxplots of the
337 initial ensemble and the updated ensemble of the source parameters for the six scenarios are
338 shown. Some observations that can be derived from this figure are: the r-EnKF (S0) produces
339 good estimates for X , Y and T with a considerable reduction of uncertainty with respect
340 to the initial ensemble, while the estimates for ΔT and M are somehow biased without a
341 large reduction of uncertainty; the ES (S1) is not effective, the spreads of the ensemble is
342 almost the same as for the initial ensemble prior to assimilation for all parameters; the ES-
343 MDA starts to work well after four iterations, and gives the best results for ten iterations,
344 outperforming the r-EnKF, particularly for parameters X , ΔT and M . The difficulty on
345 estimating ΔT and M is due to the fact that several combinations of these two parameters
346 can result in very similar sets of observations, making more difficult their identification with
347 a reduction of uncertainty. The only way to solve this indetermination is the collection of
348 additional observations. This is precisely the reason why the ES-MDA with ten iterations
349 works better than the r-EnKF for these two parameters: the r-EnKF uses all observational
350 data only once in a piecewise way, whereas the ES-MDA uses all observation data altogether
351 ten times.

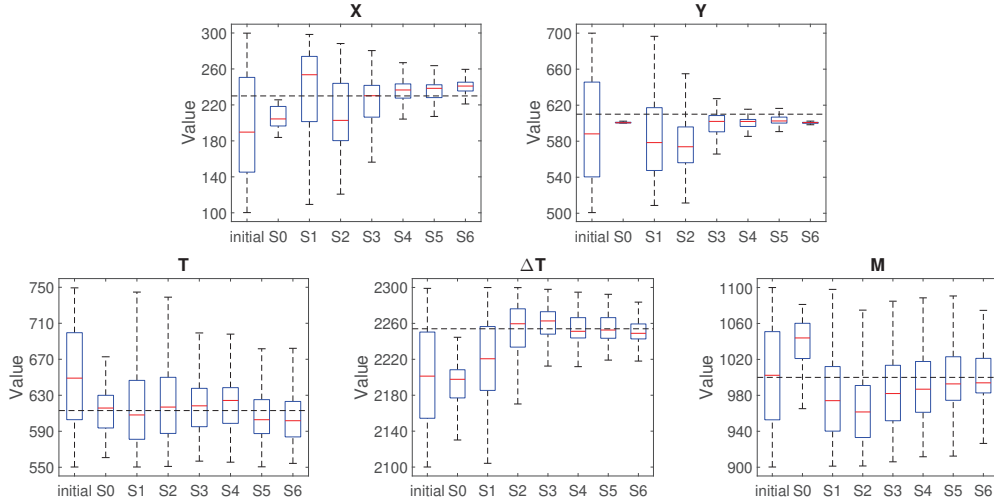


Figure 11: Scenarios S0-S6. Boxplots of the source location (X and Y), initial release time (T), release duration (ΔT), and mass-loading rate (M) computed with the initial parameters and with the updated parameters after 60 time steps. The dashed horizontal black line corresponds to the reference value.

352 5. Summary and Discussion

353 The purpose of this paper is to analyze the ability of the ES-MDA for the identification of
 354 contaminant source parameters together with a spatially heterogeneous hydraulic conductiv-
 355 ity field in comparison with the r-EnKF. The results show that the ES-MDA has the ability
 356 to estimate hydraulic conductivity field and identify the contaminant source parameters —
 357 including source location, initial release time, release duration and mass-loading rate— with a
 358 proper number of iterations, besides, the results also indicate that these estimate parameters
 359 are good enough to provide good forecasts of solute concentrations and piezometric heads.

360 It is also worth pointing out that this is the first time that the ES-MDA is applied for
 361 contaminant source identification.

362 Furthermore, the comparison over all scenarios (including also the scenarios in the ap-
 363 pendix) between the r-EnKF and the ES-MDA, shows that the ES-MDA performs better
 364 than the r-EnKF, especially for the identification of contaminant source parameters when
 365 using enough number of iterations. For the specific test done here, the ES-MDA starts to

366 outperform the r-EnKF after four iterations, needing almost the same computer time as that
367 for r-EnKF. The ES-MDA can perform even better using more iterations (and at a higher
368 computational cost). Part of the reason of the better performance of ES-MDA than of r-
369 EnKF is the fact that the number of observations is much larger for the ES-MDA, which is
370 specially important for the proper identification of mass-loading and release duration. These
371 two parameters are identified with large uncertainty by the r-EnKF.

372 It hovers over the whole paper whether an analysis on a single synthetic test case on
373 seven scenarios is sufficient to draw general conclusions about the comparison between the
374 r-EnKF and the ES-MDA. The answer is no, but drawing general conclusions was not the
375 purpose of this paper, its purpose was to test the newcomer ES-MDA against the r-EnKF in
376 a setting in which the r-EnKF had already proven to be quite effective. Given our extensive
377 experience with the application of the r-EnKF, we can forecast that a sensitivity study to
378 the number of observations will show that there is a threshold number below which it will be
379 impossible to identify the source; or that reducing the number of members of the ensemble
380 will require the use of localization and covariance inflation techniques to reach similar results,
381 with a threshold number of realizations below which identification will be impossible; or
382 that including a more uncertain prior distribution for the parameters describing the source
383 will have little impact to effectively identify the source beyond increasing the number of
384 assimilation steps.

385 While the just-mentioned sensitivity analyses are worth to carry out in a further study,
386 there is an even more interesting issue that has not been addressed neither with the r-EnKF
387 nor the ES-MDA, which is the analysis of more complex contamination events, such as
388 non-punctual or multiple source ones. Addressing these events would require a thoughtful
389 parameterization of the source.

390 **Appendix A. Results of scenarios S4 and S5**

391 Results for scenarios S4 and S5 are displayed in Figures A.12 to A.15. The details are as
392 follows: Figure A.12 shows the ensemble mean and ensemble variance of the updated $\ln K$;
393 Figure A.13 and A.14 show the 300th realization, ensemble mean and ensemble variance of
394 piezometric heads and of the contaminant plume at the end of the 60th time step, respec-
395 tively; Figure A.15 and A.16 show the time evolution of the piezometric heads and of solute
396 concentrations at the two verification wells #1, and #2 computed with the updated source
397 parameters and hydraulic conductivities.

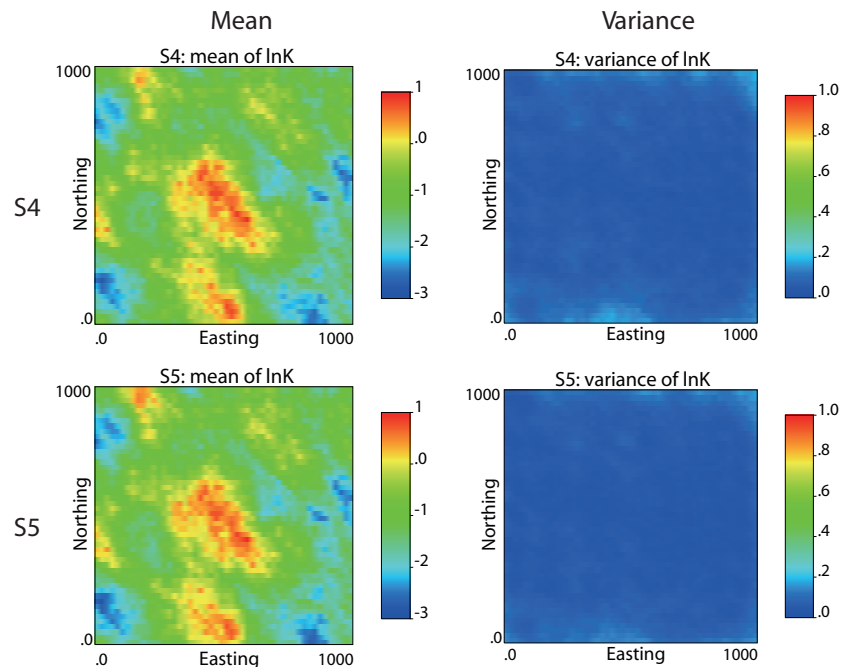


Figure A.12: Scenarios S3-S4. Ensemble mean (left column) and ensemble variance (right column) of updated log-conductivity realizations. (This figure complements Figure 4.)

398 **Acknowledgements** Financial support to carry out this work was received from the
399 Spanish Ministry of Economy and Competitiveness through project CGL2014-59841-P, and
400 from the Spanish Ministry of Education, Culture and Sports through a fellowship for the

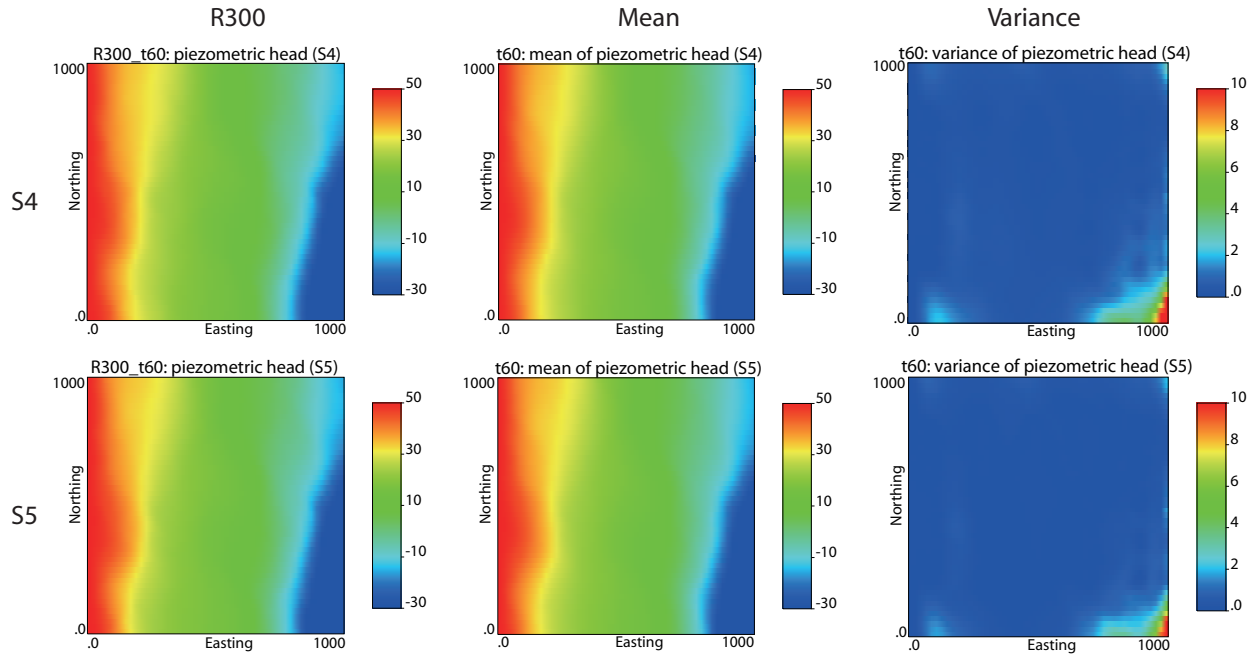


Figure A.13: Scenarios S4-S5. Piezometric heads computed with the updated parameters at the end of the 60th time step. From left to right, heads in realization #300; ensemble mean, and ensemble variance. (This figure complements Figure 6.)

401 mobility of professors in foreign research and higher education institutions of reference to
 402 the second author, reference PRX17/00150. Teng Xu also acknowledges the financial
 403 support from the Fundamental Research Funds for the Central Universities (B200201015)
 404 and Jiangsu Specially-Appointed Professor Program (B19052). Chunhui Lu acknowledges
 405 the financial support from the National Natural Science Foundation of China (51679067
 406 and 51879088), and Fundamental Research Funds for the Central Universities
 407 (B200204002).

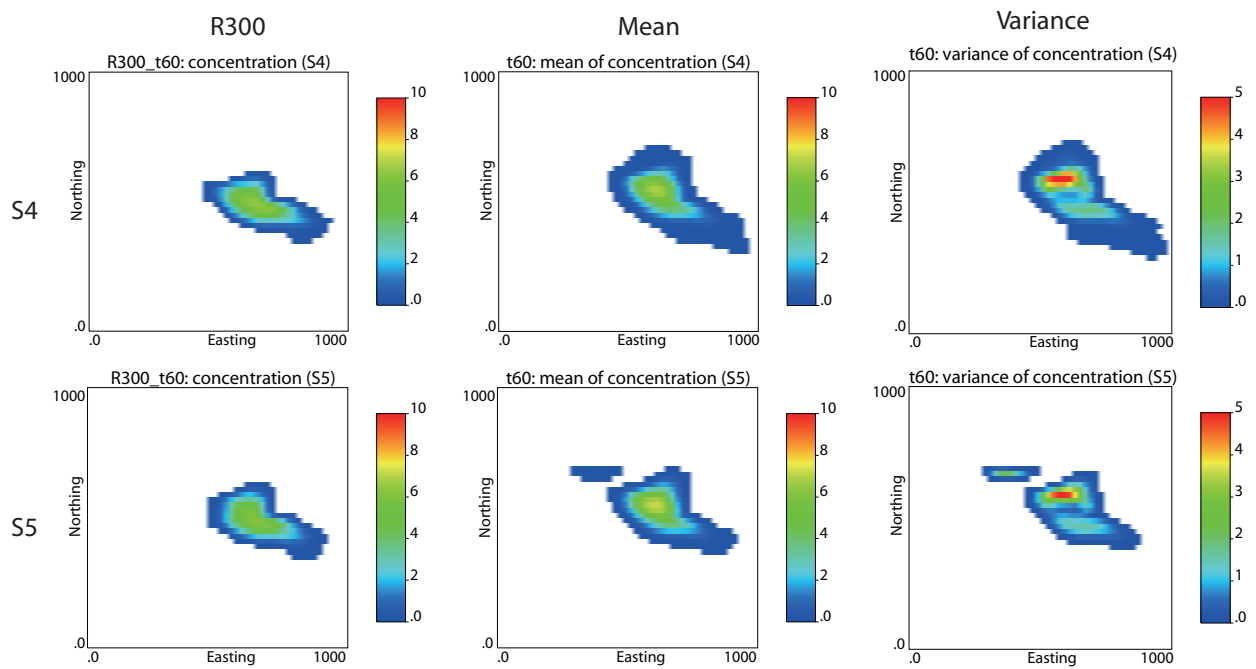


Figure A.14: Scenarios S4-S5. Contaminant plume computed with the updated parameters at the end of the 60th time step. From left to right, Contaminant plume in realization #300; ensemble mean, and ensemble variance. (This figure complements Figure 7.)

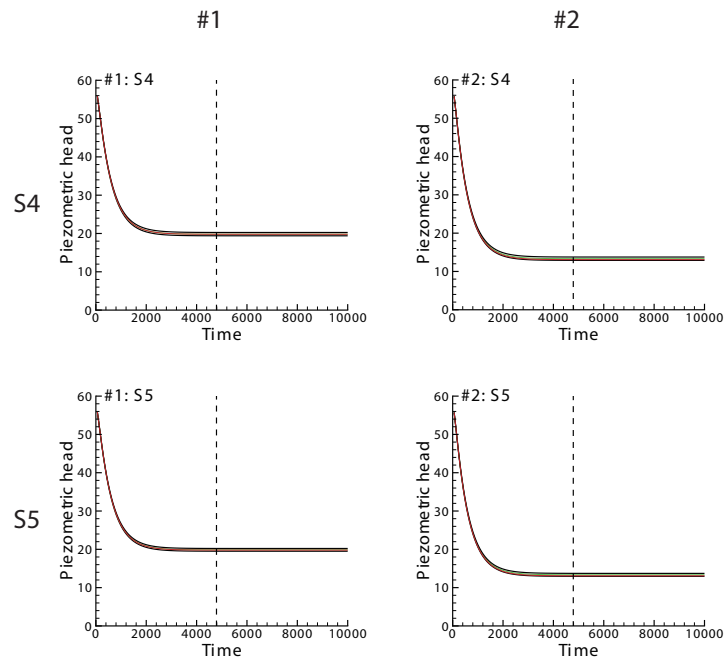


Figure A.15: Scenarios S4-S5. Time evolution of the piezometric heads at the two verification wells #1, and #2 computed with the updated ensemble of source information parameters at the end of the 60th time step. The red line is the evolution of the piezometric head in the reference. The black lines correspond to the 5 and 95 percentiles of all realizations, and the green line corresponds to the median. The vertical dashed lines mark the end of the assimilation period. (This figure complements Figure 9.)

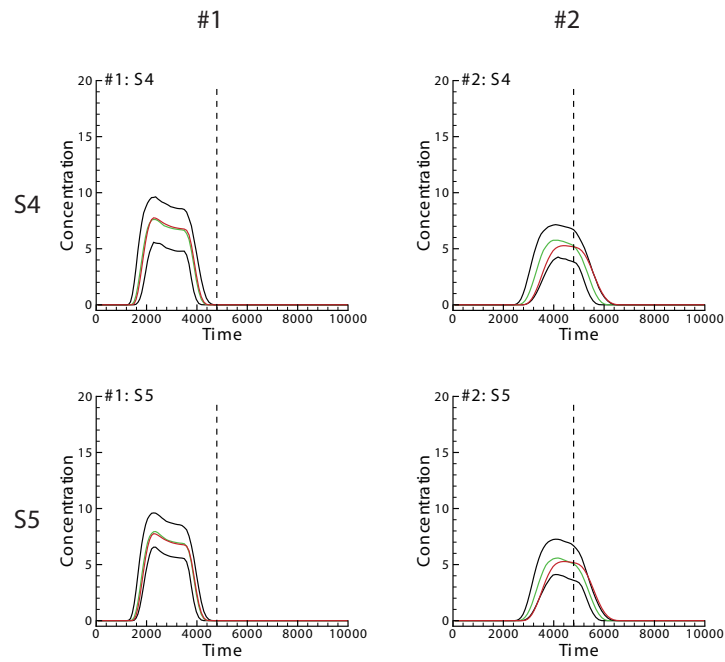


Figure A.16: Scenarios S4-S5. Time evolution of the solute concentrations at the two verification wells #1, and #2 computed with the updated ensemble of source information parameters at the end of the 60th time step. The red line is the evolution of the solute concentration in the reference. The black lines correspond to the 5 and 95 percentiles of all realizations, and the green line corresponds to the median. The vertical dashed lines mark the end of the assimilation period. (This figure complements Figure 10.)

408 **References**

- 409 Atmadja, J., Bagtzoglou, A.C., 2001a. Pollution source identification in heterogeneous
410 porous media. *Water Resources Research* 37, 2113–2125.
- 411 Atmadja, J., Bagtzoglou, A.C., 2001b. State of the art report on mathematical methods for
412 groundwater pollution source identification. *Environmental Forensics* 2, 205–214.
- 413 Ayvaz, M.T., 2016. A hybrid simulation–optimization approach for solving the areal ground-
414 water pollution source identification problems. *Journal of Hydrology* 538, 161–176.
- 415 Bagtzoglou, A.C., Atmadja, J., 2003. Marching-jury backward beam equation and quasi-
416 reversibility methods for hydrologic inversion: Application to contaminant plume spatial
417 distribution recovery. *Water Resources Research* 39.
- 418 Bagtzoglou, A.C., Atmadja, J., 2005. Mathematical methods for hydrologic inversion: The
419 case of pollution source identification, in: *Water Pollution*. Springer, pp. 65–96.
- 420 Butera, I., Tanda, M.G., Zanini, A., 2013. Simultaneous identification of the pollutant release
421 history and the source location in groundwater by means of a geostatistical approach.
422 *Stochastic Environmental Research and Risk Assessment* 27, 1269–1280.
- 423 Chen, Y., Zhang, D., 2006. Data assimilation for transient flow in geologic formations via
424 ensemble Kalman filter. *Advances in Water Resources* 29, 1107–1122.
- 425 Chen, Z., Gómez-Hernández, J.J., Xu, T., Zanini, A., 2018. Joint identification of contam-
426 inant source and aquifer geometry in a sandbox experiment with the restart ensemble
427 Kalman filter. *Journal of Hydrology* 564, 1074–1084.
- 428 Crestani, E., Camporese, M., Baú, D., Salandin, P., 2013. Ensemble Kalman filter versus
429 ensemble smoother for assessing hydraulic conductivity via tracer test data assimilation.
430 *Hydrology and Earth System Sciences* 17, 1517.

431 Cupola, F., Tanda, M.G., Zanini, A., 2015. Contaminant release history identification in
432 2-D heterogeneous aquifers through a minimum relative entropy approach. SpringerPlus
433 4, 656.

434 Emerick, A.A., Reynolds, A.C., 2013a. Ensemble smoother with multiple data assimilation.
435 Computers & Geosciences 55, 3–15.

436 Emerick, A.A., Reynolds, A.C., 2013b. Investigation of the sampling performance of
437 ensemble-based methods with a simple reservoir model. Computational Geosciences 17,
438 325.

439 Emerick, A.A., Reynolds, A.C., et al., 2013. History-matching production and seismic data
440 in a real field case using the ensemble smoother with multiple data assimilation, in: SPE
441 Reservoir Simulation Symposium, Society of Petroleum Engineers.

442 Evensen, G., 2003. The ensemble Kalman filter: Theoretical formulation and practical
443 implementation. Ocean Dynamics 53, 343–367.

444 Evensen, G., 2004. Sampling strategies and square root analysis schemes for the EnKF.
445 Ocean Dynamics 54, 539–560.

446 Evensen, G., 2009. Data assimilation: the ensemble Kalman filter. Springer Science &
447 Business Media.

448 Evensen, G., 2018. Analysis of iterative ensemble smoothers for solving inverse problems.
449 Computational Geosciences 22, 885–908.

450 Evensen, G., Van Leeuwen, P.J., 2000. An ensemble Kalman smoother for nonlinear dynam-
451 ics. Monthly Weather Review 128, 1852–1867.

452 Fokker, P., Wassing, B., van Leijen, F., Hanssen, R., Nieuwland, D., 2016. Application of
453 an ensemble smoother with multiple data assimilation to the Bergermeer gas field, using
454 PS-InSAR. *Geomechanics for Energy and the Environment* 5, 16–28.

455 Gómez-Hernández, J.J., Journel, A.G., 1993. Joint sequential simulation of Multi-Gaussian
456 fields, in: Soares, A. (Ed.), *Geostatistics Tróia '92*, Kluwer Academic Publishers, Dor-
457 drecht. pp. 85–94.

458 Gorelick, S.M., Evans, B., Remson, I., 1983. Identifying sources of groundwater pollution:
459 an optimization approach. *Water Resources Research* 19, 779–790.

460 Gu, Y., Oliver, D., 2007. An iterative ensemble Kalman filter for multiphase fluid flow data
461 assimilation. *SPE Journal* 12, 438–446.

462 Gzyl, G., Zanini, A., Fraczek, R., Kura, K., 2014. Contaminant source and release history
463 identification in groundwater: A multi-step approach. *Journal of contaminant hydrology*
464 157, 59–72.

465 Hendricks Franssen, H.J., Kinzelbach, W., 2009. Ensemble Kalman filtering versus sequential
466 self-calibration for inverse modelling of dynamic groundwater flow systems. *Journal of*
467 *Hydrology* 365, 261–274.

468 Kalman, R., et al., 1960. A new approach to linear filtering and prediction problems. *Journal*
469 *of Basic Engineering* 82, 35–45.

470 Le, D.H., Emerick, A.A., Reynolds, A.C., et al., 2016. An adaptive ensemble smoother with
471 multiple data assimilation for assisted history matching. *SPE Journal* 21, 2–195.

472 Le, D.H., Younis, R., Reynolds, A.C., et al., 2015. A history matching procedure for non-
473 Gaussian facies based on ES-MDA, in: *SPE Reservoir Simulation Symposium*, Society of
474 Petroleum Engineers.

475 Lee, K., Jeong, H., Jung, S., Choe, J., 2013. Improvement of ensemble smoother with
476 clustered covariance for channelized reservoirs. *Energy Exploration & Exploitation* 31,
477 713–726.

478 Li, L., Puzel, R., Davis, A., 2018a. Data assimilation in groundwater modelling: ensemble
479 Kalman filter versus ensemble smoothers. *Hydrological Processes* 32, 2020–2029.

480 Li, L., Stetler, L., Cao, Z., Davis, A., 2018b. An iterative normal-score ensemble smoother
481 for dealing with non-Gaussianity in data assimilation. *Journal of Hydrology* .

482 Ma, R., Zheng, C., Zachara, J.M., Tonkin, M., 2012. Utility of bromide and heat tracers
483 for aquifer characterization affected by highly transient flow conditions. *Water Resources*
484 *Research* 48.

485 McDonald, M.G., Harbaugh, A.W., 1988. A modular three-dimensional finite-difference
486 ground-water flow model. US Geological Survey.

487 Michalak, A.M., Kitanidis, P.K., 2004. Estimation of historical groundwater contaminant
488 distribution using the adjoint state method applied to geostatistical inverse modeling.
489 *Water Resources Research* 40.

490 Mirghani, B.Y., Mahinthakumar, K.G., Tryby, M.E., Ranjithan, R.S., Zechman, E.M.,
491 2009. A parallel evolutionary strategy based simulation–optimization approach for solving
492 groundwater source identification problems. *Advances in Water Resources* 32, 1373–1385.

493 Neupauer, R.M., Borchers, B., Wilson, J.L., 2000. Comparison of inverse methods for re-
494 constructing the release history of a groundwater contamination source. *Water Resources*
495 *Research* 36, 2469–2475.

496 Reynolds, A.C., Zafari, M., Li, G., 2006. Iterative forms of the ensemble Kalman filter, in:
497 ECMOR X-10th European Conference on the Mathematics of Oil Recovery.

498 Sidauruk, P., Cheng, A.D., Ouazar, D., 1998. Ground water contaminant source and trans-
499 port parameter identification by correlation coefficient optimization. *Ground Water* 36,
500 208–214.

501 Skaggs, T.H., Kabala, Z., 1994. Recovering the release history of a groundwater contaminant.
502 *Water Resources Research* 30, 71–79.

503 Skaggs, T.H., Kabala, Z., 1995. Recovering the history of a groundwater contaminant plume:
504 Method of quasi-reversibility. *Water Resources Research* 31, 2669–2673.

505 Sun, A.Y., 2007. A robust geostatistical approach to contaminant source identification.
506 *Water Resources Research* 43.

507 Sun, A.Y., Painter, S.L., Wittmeyer, G.W., 2006a. A constrained robust least squares
508 approach for contaminant release history identification. *Water Resources Research* 42.

509 Sun, A.Y., Painter, S.L., Wittmeyer, G.W., 2006b. A robust approach for iterative contam-
510 inant source location and release history recovery. *Journal of Contaminant Hydrology* 88,
511 181–196.

512 Van Leeuwen, P.J., Evensen, G., 1996. Data assimilation and inverse methods in terms of a
513 probabilistic formulation. *Monthly Weather Review* 124, 2898–2913.

514 Wang, H., Jin, X., 2013. Characterization of groundwater contaminant source using Bayesian
515 method. *Stochastic environmental research and risk assessment* 27, 867–876.

516 Woodbury, A., Sudicky, E., Ulrych, T.J., Ludwig, R., 1998. Three-dimensional plume source
517 reconstruction using minimum relative entropy inversion. *Journal of Contaminant Hydrol-
518 ogy* 32, 131–158.

- 519 Woodbury, A.D., Ulrych, T.J., 1996. Minimum relative entropy inversion: Theory and ap-
520 plication to recovering the release history of a groundwater contaminant. *Water Resources*
521 *Research* 32, 2671–2681.
- 522 Xu, T., Gómez-Hernández, J.J., 2015a. Inverse sequential simulation: A new approach for
523 the characterization of hydraulic conductivities demonstrated on a non-Gaussian field.
524 *Water Resources Research* 51, 2227–2242.
- 525 Xu, T., Gómez-Hernández, J.J., 2015b. Probability fields revisited in the context of ensemble
526 Kalman filtering. *Journal of Hydrology* 531, 40–52.
- 527 Xu, T., Gómez-Hernández, J.J., 2016. Joint identification of contaminant source location,
528 initial release time and initial solute concentration in an aquifer via ensemble Kalman
529 filtering. *Water Resources Research* 52.
- 530 Xu, T., Gómez-Hernández, J.J., 2018. Simultaneous identification of a contaminant source
531 and hydraulic conductivity via the restart normal-score ensemble Kalman filter. *Advances*
532 *in Water Resources* 112, 106–123.
- 533 Xu, T., Gómez-Hernández, J.J., Zhou, H., Li, L., 2013. The power of transient piezometric
534 head data in inverse modeling: An application of the localized normal-score EnKF with
535 covariance inflation in a heterogenous bimodal hydraulic conductivity field. *Advances in*
536 *Water Resources* 54, 100–118.
- 537 Zanini, A., Woodbury, A.D., 2016. Contaminant source reconstruction by empirical Bayes
538 and Akaike’s Bayesian Information Criterion. *Journal of contaminant hydrology* 185, 74–
539 86.
- 540 Zeng, L., Shi, L., Zhang, D., Wu, L., 2012. A sparse grid based Bayesian method for
541 contaminant source identification. *Advances in Water Resources* 37, 1–9.

- 542 Zhang, J., Zeng, L., Chen, C., Chen, D., Wu, L., 2015. Efficient Bayesian experimental
543 design for contaminant source identification. *Water Resources Research* 51, 576–598.
- 544 Zheng, C., 2010. Technical Report. Technical Report to the US Army Engineer Research
545 and Development Center.